THE JOURNAL OF PHYSICAL CHEMISTRY C
A JOURNAL OF THE AMERICAN CHEMICAL SOCIETY

pubs.acs.org/JPCC

Article

Understanding Anomalous Gas-Phase Peak Shifts in Dip-and-Pull Ambient Pressure XPS Experiments

Detre Teschner,* Julius Plescher, Simone Piccinin, Travis E. Jones, Adnan Hammud, Franz Schmidt, Axel Knop-Gericke, Hendrik Bluhm, and Andrey Shavorskiy

Cite This: J. Phys. Chem. C 2024, 128, 7096–7105

Read Online

ACCESS | Metrics & More | Article Recommendations | Supporting Information

ABSTRACT: Dip-and-pull ambient pressure X-ray photoelectron spectroscopy (AP-XPS) holds promise to uncover elementary processes of (photo)electrochemistry. We show, however, that the sample for such experiments should preferably be nonporous and the potential on the surface homogeneous. We carried out dip-and-pull AP-XPS experiments on a hematite thin film sample under the photoelectrochemical oxygen evolution reaction (OER) and find unexpected O 1s core level shifts. Upon electrochemical biasing under simulated solar light illumination, the gas-phase water peak shifted more than the electrolyte peak. To uncover the origin of the unexpected larger shift of the gas-phase peak, we performed electrostatic simulations using COMSOL, to map the potential field in the relevant volume between the sample and the first aperture of the XPS spectrometer. A number of geometric models were considered. We find that when the potential on the sample surface is inhomogeneous, e.g., with ionically isolated electrolyte patches, the gas-phase peak of the spectrum can shift more than the peak due to the electrolyte film. This suggests that at the measured sample position, the local potential was not as set by the potentiostat. Despite this, we find reversible consumption and replenishment of hydroxide in the spectra, which, due to OH^- being the reactant of the OER in alkaline electrolyte, makes sense chemically. We propose that this is linked to OH^- diffusion across the measured sample position, driven by the potential dependent consumption and replenishment of OH^- at the nearby well-connected surface regions.

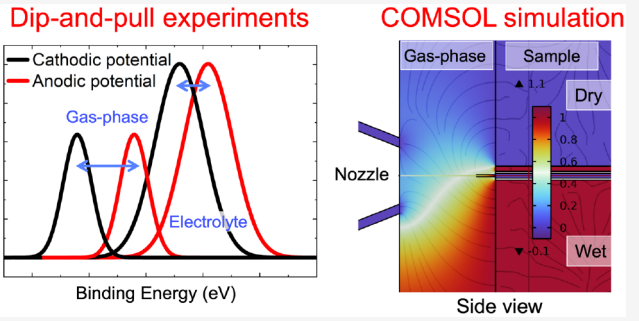

INTRODUCTION

Researchers and scientific journals prefer to report successful studies, often ignoring negative results.[1] Hence, negative results are disappearing from most disciplines.[2] This narrow and skewed display of research hinders the development of science and makes systematic reviews and meta-analyses ever more difficult.[3,4] Reporting negative results helps scientists to identify potential confounding factors and prevent repeating the same mistakes, and it can help to avoid wasting financial and personal resources. Therefore, both positive and negative results are crucial for balanced and credible scientific progress. In this paper, we report on an unexpected negative result within a seemingly successful experiment, explore the reasons for this result through a set of simulations, and provide a sound explanation as to why the experiment ultimately failed.

The topic of this article is a dip-and-pull ambient pressure X-ray photoelectron spectroscopy (AP-XPS) experiment on a hematite photoanode under oxygen evolution reaction (OER) conditions. This anodic half reaction of the overall (photo) electrochemical water splitting is the bottleneck to produce "green" hydrogen. The OER is also a key process in natural photosynthesis. Due to its significance in different fields of chemistry, the OER is studied by different communities (e.g., biochemists, synthetic photochemists, electrochemists, and material scientists); more often than not, each community fails to recognize the advances achieved by the other communities. This leads to a widespread of mechanistic understanding for the same reaction across bio-, photo-, and electrocatalysts and even to diverse semantics used by these different chemical communities.

Hydrogen is considered to be a major component as a chemical storage material in the transition to utilize renewable energy resources. The synthetic OER is a vast field of research, on the one hand targeting the exploration of new, efficient, and/or cheap (photo) electrocatalysts and on the other hand focusing on the understanding of the reaction mechanism at the molecular level. Given the vast number of articles on this topic, it is impossible to give a complete introduction to this field; we thus provide a targeted description of the motivation

Received: January 6, 2024
Revised: April 9, 2024
Accepted: April 10, 2024
Published: April 22, 2024

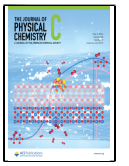

for the AP-XPS experiments in the next paragraph and point the interested reader to a few recent review papers on the wider topic.[5−13]

While studying the OER under acidic conditions over iridium-based electrocatalysts, we have recently found that electron transfer steps are largely equilibrated and that a purely chemical O−O bond formation step mediates the overall OER rate for a range of catalysts and conditions.[14] In such cases, the applied electrochemical potential acts to form the active surface phase, which can be measured by way of operando X-ray absorption and photoemission spectroscopy techniques. We have also shown how the electrocatalytic OER potential induced changes in the average oxidation state of the active surface, which influence the activation energy of the chemical O−O coupling step through a linear free energy relationship similar to what is known from thermal catalysis. This gives rise to an exponential dependence of the OER rate on the oxidative charge stored in the material, which can be measured in the laboratory by pulse voltammetry. This view was novel for electrocatalysis but is, however, somewhat similar to what was proposed for bio- and photochemical OER. In a more recent publication, we have shown how a similar picture emerges for the photoelectrocatalytic OER over hematite, where the OER rate is again controlled by the total charge stored in the catalyst.[15] In this case, however, in situ transient photocurrent measurements under chopped illumination in conjunction with density functional theory simulations revealed that a power rate law emerges due to the participation of multiple near-surface electron holes in a chemical O−O coupling step. Such a power rate law was also found for a number of other photoanodes.[16,17] These localized hole states at the surface of hematite are predicted to be shared between Fe and O ions in an antibonding orbital.[15] Operando infrared experiments suggested a similar iron−oxo intermediate.[18] We note here that hole states (partially) centered on oxygen were also found in hematite under simulated solar illumination using X-ray absorption spectroscopy by measuring the total fluorescence yield.[19]

To study these surface hole states experimentally, a natural choice is ambient pressure X-ray photoelectron spectroscopy since XPS is intrinsically sensitive to the near-surface region of a solid sample. Some of us previously performed a dip-and-pull AP-XPS study on hematite under varying electrochemical conditions, in which no Fermi level pinning and no surface states over the potential range of 0.4−1.2 eV below the conduction band were found.[20] The goal of this study was to perform a similar experiment on the same photoanode as used in our transient photocurrent measurements. Hence, to falsify or verify the lack of surface states found in ref 20, and in the former case to identify their spectroscopic signature and to correlate their surface concentration with the photoelectrocatalytic OER rate. We were ultimately not able to draw these correlations due to artifacts that we encountered in the experiments, and we decided to investigate these artifacts further. Through simulations of the electrostatic potentials at the sample surface and in the gap between the sample and the differentially pumped aperture, we are able to explain these artifacts in the observed peak shifts as a function of the applied potential. We believe that these effects, which are caused by inhomogeneous wetting and the nanoscale morphology of the sample, are potentially present in a wide range of dip-and-pull experiments. Owing to the growing popularity of this experimental technique, we find it prudent to describe these possible pitfalls in detail.

METHODS

Sample Preparation. The sample S10 used in this work was described in ref 15. Briefly, its preparation consisted of two major steps. (1) Anodic electrodeposition of an iron oxyhydroxide onto an FTO-coated glass was carried out in a plating solution of 16 mM $(NH_4)_2Fe(SO_4)_2$, 2.4 M $(NH_4)_2SO_4$, and 2 mM H_2SO_4 in ultrapure water at −0.1 V vs Ag/AgCl after adjusting the pH to 7.5 by adding KOH solution. (2) After rinsing and drying, the sample was annealed for 20 min at 800 °C in air. A similar sample S2 was also prepared, with an identical procedure, with only the deposited charge and hence its hematite loading was 20% S10.

Transmission Electron Microscopy. A focused ion beam (FIB) lamella was prepared with a Thermo Fisher Scientific FIB/SEM DualBeam Helios NanoLab G3 UC device. Transmission electron microscopy images were measured with a Thermo Scientific Talos F200X microscope equipped with an X-FEG field emission gun.

Ambient Pressure X-Ray Photoelectron Spectroscopy. Dip-and-pull AP-XPS experiments were carried out at the MAX IV Laboratory using the electrochemical/liquid cell as the sample chamber at the HIPPIE beamline.[21,22] A fixed excitation energy of 1600 eV was used in this work. The beamline during the experiments had an energy offset of approximately −1.3 eV at this photon energy. Therefore, the binding energy in all spectra we show were corrected by +1.3 eV. Different exit slit and pass energy combinations were tested during the experiments. A 100 μm exit slit was used for sample S10, whereas it was decreased to 25 μm for sample S2. The photon flux at 1600 eV and 50 μm slit is 8×10^{11} photons/s and scales linearly with the slit size. The theoretical resolving power is 7000 at 1600 eV and a 25 μm slit, which results in approximately 230 meV beamline contribution to peak broadening. For a 100 μm slit, we have 1700 resolving power, which at 1600 eV results in a slightly less than 1.0 eV beamline contribution. All dip-and-pull O 1s spectra shown in this article were recorded with 100 eV pass energy. The beam size on the sample was 80 μm × 40 μm (width × height), independent of the slit size. The incident angle is 55° with respect to the surface normal. Working distance is approximately 450−500 μm. The sample chamber contained a beaker on a holder with 0.1 M KOH and an electrode housing on a manipulator holding the three electrodes dipped in the electrolyte. The hematite samples on FTO (S10 and S2) were our working electrodes, while a Pt foil served as a counter electrode and a leakless Ag/AgCl as a reference electrode. The electrolyte was degassed in a separate chamber prior to introduction into the sample chamber. The beaker holder is cooled to 6−10 °C to reduce the equilibrium vapor pressure in the chamber. The chamber is additionally pumped mildly to maintain a fixed water vapor pressure of 13−15 mbar. A Biologic SP-200 potentiostat was used to control the applied potential to the working electrode, of which back-contact was grounded together with the XPS spectrometer. The sample was illuminated with an AM 1.5G simulated sunlight (Asahi Spectra HAL-320 solar simulator placed ca. 20 cm away from sample at ∼50 deg incidence angle) via quartz viewport.

COMSOL Simulation. We used the AC/DC Module of COMSOL Multiphysics software to perform the modeling.[23]

https://doi.org/10.1021/acs.jpcc.4c00113
J. Phys. Chem. C 2024, 128, 7096−7105

Specifically, the electrostatic interface was utilized to compute the electric field in a number of geometric models. The interface solves Gauss' Law for the electric field using the scalar electric potential as the dependent variable. The purpose of these simulations was to understand the potential distribution in space resembling the geometry in the AP-XPS experiment. To do so, we built a simple general model consisting of a sample (3 × 2 × 1 mm) and a cone (bottom radius: 0.2 mm, top radius: 1 mm, wall thickness: 0.05 mm, height: 2 mm). The bottom part of the cone faces the sample at a distance of 0.5 mm. The cone is always on the ground potential and represents the nozzle (spectrometer entrance aperture) in the experiment. In the simulation, both the sample and cone are built from copper and the space between them is filled with air, but the choice of material is irrelevant for the simulation. A small volume of 0.1 × 0.1 × 0.01 mm directly in front of the sample, on the common horizontal axis of the cone and sample, was defined to calculate the average potential of this volume (Domain Probe) as an approximation for the average gas-phase binding energy shift in the AP-XPS experiment. Also, the potential field between the sample and cone was sampled by a line scan (Line Segment), on the common horizontal and vertical axes of the sample and cone. Three specific models were built.

Model1. The sample was divided into two parts: a lower (ionically conductive and wet part in experiment) and an upper (nonconductive and dry part in experiment), and their potentials were set to 1 and 0.02 V, respectively. To simulate the influence of the position of the wet/dry boundary, the whole sample was moved up/down with respect to the fixed Domain Probe.

Model2. Here, we start with an undivided sample on 1 V. Then, we introduce on the common horizontal and vertical axis of the sample and cone a hole in the sample and the hole is almost completely filled with a rod, with a separation of 0.01 mm. The rod is set to an arbitrarily low potential, 0.02 V, and its front surface represents an isolated patch in the experiment. The size of the rod was varied, the front surface being 0.05 × 0.025 mm, 0.2 × 0.1 mm, or 0.8 × 0.4 mm, all having a 2 × 1 width/height ratio. The same calculation was also performed with square type front surfaces having the same surface areas as described above, with practically identical results.

Model3. In this model, Model1 and Model2 were combined, in which the isolated patch with the smallest size (0.05 mm × 0.025 mm) was introduced into the wet sample part of Model1, 0.05 mm below the wet/dry interface.

RESULTS AND DISCUSSION

Dip-and-pull AP-XPS experiments were recently implemented at numerous synchrotrons, for example at the ALS,[24,25] SLS,[26] MAX-IV[21,22] and BESSY-II.[27] In such experiments, a three-electrode system with the electrolyte and a beaker is placed in the sample chamber of the AP-XPS spectrometer.

Figure 1 shows a photo with the main components of the dip-and-pull experiment that we discuss in the following. The sample (working electrode) and the counter and reference electrodes are mounted in an electrode housing on a manipulator that can be rotated and moved in X/Y/Z directions, and they are connected to a potentiostat. The beaker with the electrolyte (0.1 M KOH) can also be moved in X/Y/Z. As a sample, we used a glass wafer, with one side coated in F-doped tin oxide (FTO) and covered by a thin hematite film. This appears in the photograph as a yellow/orange tint on the lower part of the wafer. The sample back-contact is on a common ground potential with the spectrometer and its first aperture. The sample is immersed into and slowly pulled from the electrolyte ("dip-and-pull") to form a meniscus of the liquid electrolyte film on the sample surface. When done properly and the sample is sufficiently hydrophilic and in close equilibrium with the vapor pressure of the solution, the thin electrolyte film should be ionically connected with the bulk of the electrolyte. The sample is then moved close to the entrance aperture of the spectrometer ("nozzle") to be in the common focus of the X-ray beam and the electron analyzer. As a final step, the sample is moved up/down to find a proper position where both the (major) electrolyte and the (minor) sample signatures are visible in the XP spectrum. For photoelectrochemical experiments, the sample can be illuminated, in our case with an AM 1.5G simulated sunlight mounted on a quartz viewport.

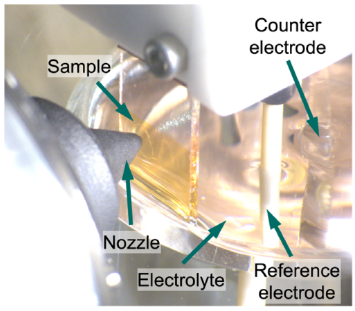

Figure 1. Annotated photograph of the dip-and-pull setup inside the spectrometer sample chamber. The nozzle is the entrance aperture to the spectrometer.

Figure 2A shows the O 1s spectra of the hematite sample S10 (film thickness: 200 nm) under ultrahigh vacuum (UHV; before introducing the electrolyte into the sample chamber) and in water vapor (before immersing the sample into the electrolyte). The intensity was scaled and the spectra were fit

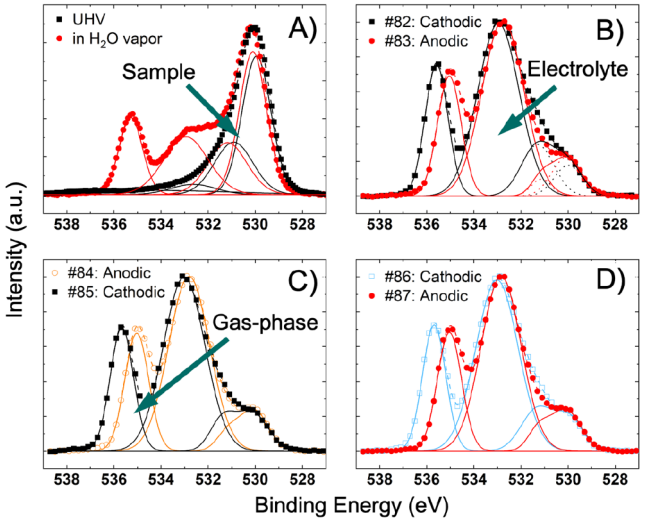

Figure 2. O 1s spectra of sample S10 (symbols) under various conditions: A) under UHV and in H_2O vapor before immersion into the 0.1 M KOH electrolyte. B–D) A set of dip-and-pull spectra under anodic (1.6 V vs reversible hydrogen electrode or RHE) or cathodic (0.6 V vs RHE) polarization. A solar simulator is turned on in B–D). Photon energy: 1600 eV. Exit slit: 100 μm.

https://doi.org/10.1021/acs.jpcc.4c00113
J. Phys. Chem. C 2024, 128, 7096–7105

with Gauss−Lorentz profiles. The O 1s spectrum in a vacuum (Figure 2A) contains one major peak due to lattice oxygen (529.95 eV binding energy, BE) and an asymmetric tail to the higher binding energy side, assigned to surface OH (530.91 eV) and surface water (532.63 eV). Because the electrolyte beaker is cooled to 15−17 °C, a close-to-equilibrium gas-phase pressure of 13−15 mbar is reached with a very mild pumping of the sample chamber. The gas-phase water vapor peak is at close to 535.2 eV BE in the spectrum before immersion of the sample into the liquid. At this vapor pressure of water, an increased adsorbed water peak (532.94 eV) signals multilayer water on the surface of the sample. Overall, the lattice oxygen and surface OH peaks are approximately 0.2 eV upshifted with respect to the UHV spectrum, suggesting that multilayer water adsorption changes the band bending of the sample, giving rise to the apparent binding energy shift.

Figure 2B−D shows a representative set of the O 1s spectra under solar illumination and applied potentials between anodic (1.6 V) and cathodic (0.6 V) conditions; all potentials are vs RHE. An extended version of the figure is shown in Figure S2, with anodic and cathodic conditions repeated before reversing polarization to show (1) the reproducibility and (2) any minor temporal evolution in the data. The set starts with spectrum #82 at 0.6 V, dominated by the gas-phase (535.59 eV) and the electrolyte (532.96 eV) peaks. The two lower binding energy peaks previously assigned to lattice O and surface OH are also present, but their exact deconvolution is complicated and depends strongly on the boundary conditions used in the fitting procedure, due to their lower intensity and their partial overlap with the electrolyte peak. Their sum, however, can be estimated with high precision, because the line shape of the electrolyte peak is rather insensitive to the fit boundary conditions. In Figure 2B, the two low binding energy components are depicted as dotted lines, and their sum is depicted as a full line. In the remaining spectra, only their sum is shown, as it conveys the necessary information.

When the sample is anodically biased (no. 83, 1.6 V), the spectrum shifts to lower binding energies, though the magnitude of the shifts is different. We note that under these conditions the sample evolves oxygen, as shown by the enhanced current in the cyclic voltammetry curve (Figure S1). At a bias of +1 V, the gas-phase peak shifts to a 0.55 eV lower BE, the electrolyte peak shifts to a 0.19 eV lower BE, and the lattice O shifts even less (if at all). The peak previously assigned to surface OH clearly loses intensity; its relative spectral weight in the fit decreases from 13% to an estimated 3%. Next, the same anodic condition was repeated (Figure S2C), and the spectrum is well reproduced, without significant changes in the peak positions or intensities. Thereafter, the potential is reversed back to 0.6 V (Figure 2C), upon which the gas-phase and electrolyte peaks shift roughly back to their original positions, whereas the surface O peak is unshifted. Under these cathodic conditions the peak at approximately 531.5 eV increases slightly in intensity. Repeated acquisition at 0.6 V (Figure S2E) does not change the spectrum except that the 531.5 eV peak shows a slight further increase in intensity. Finally, when the polarization is changed back to anodic, the peaks shift back toward lower BEs. The exact peak shifts are summarized in Table 1. Another very similar set of spectra with the same observations can be found in Figure S3. Hence, the sample in this experiment showed reproducible responses to variations in the applied potential. However, the observation of larger gas-phase peak shifts compared to those of the electrolyte is unexpected, as we explain in the following. We note that the observation is not related to the presence of the simulated sunlight irradiation because similar unexpected binding energy shifts were also found under dark conditions, not shown. We estimated the electrolyte film thickness using the inelastic mean free path (IMFP) of electrons in liquid water[28,29] and the electrolyte-to-lattice O 1s peak areas in Figure 2. Assuming an IMFP of ∼4 nm and an average electrolyte-to-lattice oxygen ratio of 7.5, the average electrolyte thickness is around 8 nm, i.e., sufficiently thick to form an electrical double layer. Finally, similar larger-than-expected gas-phase shifts in dip-and-pull experiments can be found in the literature,[30] though the authors of that study did not discuss this particular aspect of their results.

Table 1. Gas-Phase and Electrolyte Binding Energy Shifts with Sample S10, Corresponding to Figure 2

	gas-phase shift (eV)	electrolyte shift (eV)
#82 (cathodic) to #83 (anodic)	−0.55	−0.19
#84 (anodic) to #85 (cathodic)	0.63	0.21
#86 (cathodic) to #87 (anodic)	−0.65	−0.18

Before discussing the origin of the unexpected peak shifts in the experiments in Figure 2, we present results of a dip-and-pull experiment on a different sample (sample S2) that had a hematite loading of only 20% of sample S10. While this sample also provided similar results to those in Figure 2 at some sample locations, it showed the expected behavior in some other areas. One of these data sets is reproduced in Figure 3, and another is in Figure S4. Spectrum #76 was taken at 0.6 V and clearly shows the electrolyte peak and the 531.5 eV component, while the lattice O peak is very weak, if present at all. Upon anodic polarization (+1.6 V), the gas-phase peak shifts by −0.87 eV, the electrolyte by −0.95 eV and the 531.5 eV component by −0.88 eV. Of note, upon 1 V extra bias, the electrolyte peak now shifts by roughly −1 eV, and the gas-phase peak shifts less than the electrolyte peak. From Figure 3B, the polarization is reversed back to cathodic, giving rise to the corresponding positive peak shifts, as conveyed in Table 2. Upon switching back to anodic polarization (Figure 3C), the gas-phase and electrolyte peaks shift reversibly again. Hence, in all of these measurements shown in Figure 3, the electrolyte peak shifts are always close to ±1 eV, in line with the ±1 V biasing (changing between 0.6 and 1.6 V), and the gas-phase peak shifts less. The ±1 eV electrolyte shift upon ±1 V biasing is in agreement with the assumption that the meniscus is ionically well connected to the bulk of the electrolyte and that the electrochemical double layer contribution with a potential drop is negligible in the probed electrolyte volume.

To understand why the O 1s core level shifts in response to changing potentials observed in Figure 2 are unexpected, we consider the geometry and the energy diagram of the sample−spectrometer first aperture region (Figure 4). When the incident X-ray beam irradiates the sample surface and the sample is in a gaseous environment, part of the gas phase that is in the beam path and within the acceptance angle of the electrostatic lens system of the spectrometer will also contribute to the spectrum. This is schematically shown as the purple area in Figure 4A. With a conductive sample, the binding energy of surface species is typically referenced to the Fermi level (E_F) of the sample, which is equal to that of the spectrometer, because the sample is on common ground with

https://doi.org/10.1021/acs.jpcc.4c00113
J. Phys. Chem. C 2024, 128, 7096−7105

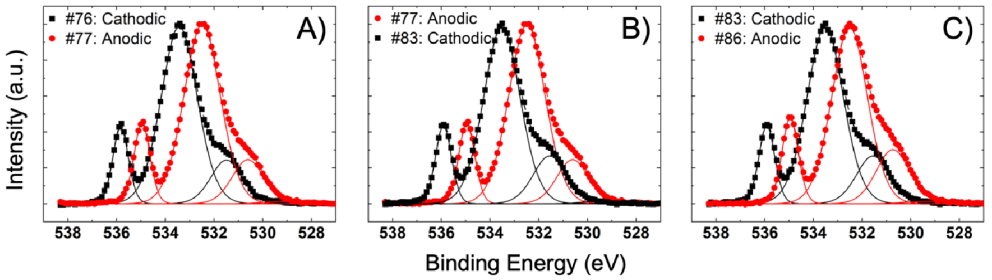

Figure 3. Dip-and-pull O 1s spectra of sample S2 under anodic (1.6 V vs RHE) and cathodic (0.6 V vs RHE) polarization. The solar simulator is turned on. Photon energy: 1600 eV. Exit slit: 25 μm.

Table 2. Gas-Phase and Electrolyte Binding Energy Shifts with Sample S2, Corresponding to Figure 3

	gas-phase shift (eV)	electrolyte shift (eV)
#76 (cathodic) to #77 (anodic)	−0.87	−0.95
#77 (anodic) to #83 (cathodic)	0.95	1.03
#83 (cathodic) to #86 (anodic)	−0.86	0.92

the spectrometer. The gas-phase peaks are, however, usually referenced to the vacuum level (E_{vac}), see Figure 4B. In our dip-and-pull experiments, a thin electrolyte film covers the sample surface, and its potential, if the layer is ionically connected to the bulk of the electrolyte, is controlled by the potentiostat. When the sample is metallic, the full potential drop occurs in the Helmholtz double layer. When the sample is a semiconductor, as in the case of hematite, the full potential drop is divided between the Helmholtz double layer and the space charge layer in the semiconductor. A ±1 V biasing can give rise to a maximum 1 eV shift of the apparent binding energy of the electrolyte peak. The actual binding energy shift of the electrolyte can be between 0 and 1 eV and will depend on a number of conditions, as explained in the Supporting Information. When the vacuum level of gas phase (E_{vac}^{sam}) couples to the electrolyte surface (E_{vac}^{liq}) and to the fixed potential of the grounded spectrometer aperture (E_{vac}^{ap}), the gas-phase binding energy shift is necessarily lower than the electrolyte binding energy shift upon biasing the electrolyte potential, as indicated in Figure 4B. This is because the gas-phase signal is mainly detected from the space in between the aperture and the sample, where the observed gas-phase peak shift depends on, e.g., the cross section and the orientation of the incident X-ray beam. This picture is consistent with the observations in the O 1s spectra in Figure 3, but not with those in Figure 2. To investigate the possible reasons as to why a gas-phase peak may shift more than that of the electrolyte, we carried out a number of electrostatics simulations in COMSOL[23] to evaluate the electric field and potential distribution in the space between the sample and the fist aperture of the spectrometer.

The AC/DC Module of COMSOL was used to compute the potential distribution within a number of geometric schemes including varying sample homogeneity. We start with the model depicted in Figure 5A. The left side shows that the sample is divided into two parts: the lower part is assumed to be covered by an electrolyte ("Wet"), with the potential set to +1 V, representing a 1 V bias in the experiments. The upper part of the sample is assumed to be dry, that is, ionically not connected to the lower part. We assign the potential of this sample part to an arbitrary low number, 0.02 V in the present case. The entrance aperture of the spectrometer (nozzle) is on the right side of Figure 5A; as in the experiment it is on ground potential. It has an aperture diameter of 0.3 mm and a wall thickness of 0.05 mm, with a distance of 0.5 mm to the sample surface. These boundary conditions are reasonable estimates of typical AP-XPS experiments. The space between the sample and the nozzle is filled with gas. In the simulation, it is air, but the actual nature of the gas does not play a role in the simulation results.

To approximate the average gas-phase peak shift measured in the experiment, a small volume in front of the sample was defined to probe the average potential in this segment, i.e., in

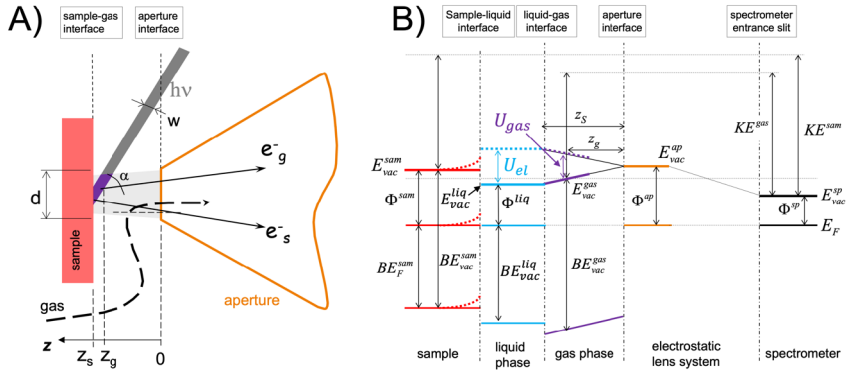

Figure 4. A) A simplified geometric scheme of the sample−spectrometer first aperture region. B) Energy diagram of the sample, gas and liquid phase, and spectrometer. U_{el} indicates the external bias by a potentiostat to the electrolyte covered sample surface; U_{gas} is the expected shift of the gas-phase potential. *E*: energy, BE: binding energy, KE: kinetic energy, Φ: work function, subscripts F and vac are for Fermi and vacuum levels, and superscripts emphasize the objects the energy levels are referring to. Adapted from ref[31]. Copyright 2010 Elsevier.

https://doi.org/10.1021/acs.jpcc.4c00113
J. Phys. Chem. C 2024, 128, 7096−7105

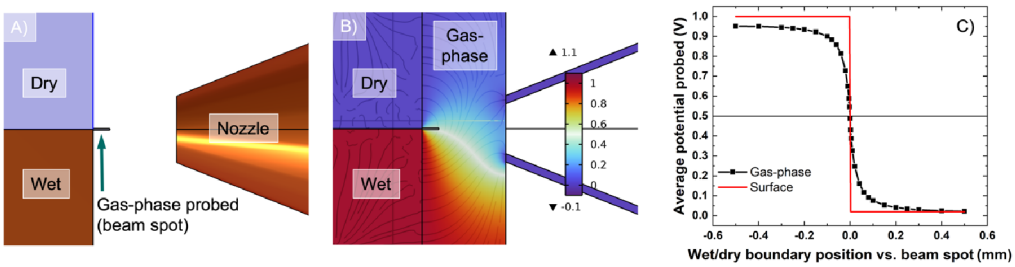

Figure 5. A) Side view of a geometric scheme (Model1) simulated in COMSOL. The sample has two parts: the lower part is assumed to be wet with a potential set to +1 V, and the upper part is dry and is at a potential of 0.02 V. The spectrometer's first aperture (nozzle) is on ground potential. The space between the sample and nozzle is filled with gas and a small segment of it (0.1 × 0.1 × 0.01 mm) is probed, similar to AP-XPS. The incoming X-rays are on the horizontal axis of the nozzle. B) Color plot of the electric potential distribution in the simulated space at the vertical axis of the nozzle; side view. C) To simulate the influence of the position of the wet/dry boundary, the whole sample was moved up/down. The plot in C) shows the average potential probed on the surface and in the small gas-phase segment depending on the wet/dry boundary position with respect to the fixed beam spot.

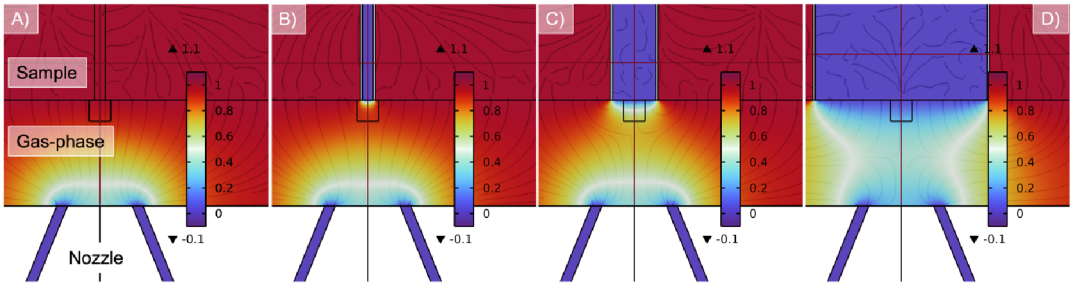

Figure 6. A–D) Color plots of the electric potential distribution in the simulated space for Model2 at the horizontal axis of the nozzle; top view. In A) the whole sample is undivided and its potential is set to 1 V. In B–D) we introduce an isolated patch with varying sizes; its horizontal axis is placed on the axis of the nozzle and its potential is 0.02 V. Patch size (from left to right): 0.05 × 0.025, 0.2 × 0.1, and 0.8 × 0.4 mm. The sampled gas segment is also shown as a black square (0.1 mm × 0.1 mm) in front of the sample.

this volume, the incident X-rays and the analyzer acceptance volumes intersect. The results of the simulation are depicted in Figure 5B,C. Figure 5B shows the electric potential distribution as a color plot, whereas Figure 5C illustrates the average potential probed in the gas phase and also on the surface when the whole sample and accordingly the wet/dry boundary position are moved up or down with respect to the fixed beam spot. We can make a number of observations from these results. First, evidently both parts of the sample have a strong influence on the potential field, with strong local changes close to the wet/dry interface and increasing intermixing of the potentials with increasing distance from the sample surface. Second, the nozzle potential plays an important role in the potential distribution between the sample and nozzle, as well. Of note how the average potential region (0.5 V, white area) is spatially deflected from the horizontal (symmetry) axis toward the area below the nozzle, i.e., over the wet part of the sample. Third, the approximation of the gas-phase potential between the sample and nozzle with a linear dependence, as in Figure 4B, is not completely wrong, but it is an oversimplification. Lastly, as the average probed potential plot shows, the gas-phase follows the surface potential, but due to the influence of the dry part of the sample and the nozzle, the potential curve is much smoother than the surface potential. Although the gas-phase potential approaches the surface potential of 1 V, it never reaches 1 V due to the effect of the nozzle. Hence, the gas-phase potential shifts are always smaller than the surface potential shifts. The results clearly indicate that with this model, we cannot explain the larger shift of the gas-phase with respect to that of the electrolyte, as discussed in Figure 2.

Our next model is an isolated sample patch on an otherwise ionically well-connected and conductive sample surface (Figure 6), where the patch is represented in the 3D model by an electrically isolated rod. Figure 6 shows the dependence of the potential distribution as a function of changing the size of the isolated patch with no isolated patch in Figure 6A and a gradually increasing size of the patch in Figure 6B–D. Figure 7

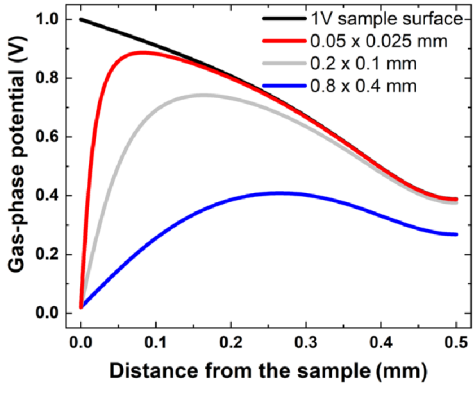

Figure 7. A line scan plot of the gas-phase potential in Model2, for the 4 cases shown in Figure 6. The line scan is between the sample and the nozzle along the vertical line passing through the center of the nozzle; see Figure 6, which is the common horizontal and vertical axis of the isolated patch and the nozzle. The 1 V sample surface is the case of no isolated patch. A similar line scan plot is shown in Figure S5 for a square type patch instead of the 2 × 1 quad, with practically identical results.

https://doi.org/10.1021/acs.jpcc.4c00113
J. Phys. Chem. C 2024, 128, 7096–7105

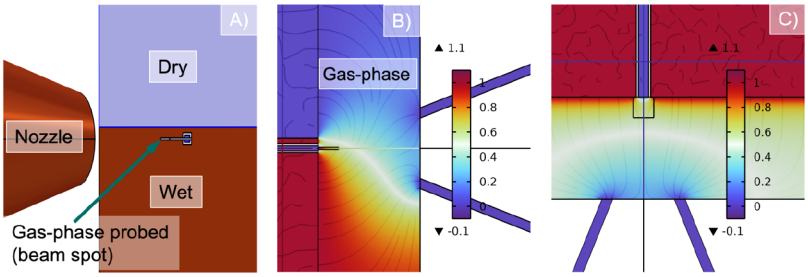

Figure 8. A) Diagonal side view of a geometric scheme (Model3) simulated in COMSOL. The sample has two parts: the lower part is assumed to be wet with a potential set to +1 V, and the upper part is dry and is at a potential of 0.02 V. Inside the wet area a small isolated patch (with the size as in Figure 6B) is introduced. The spectrometer's first aperture (nozzle) is on ground potential. The space between the sample and nozzle is filled with gas and a small segment of it (0.1 × 0.1 × 0.01 mm) is probed, similar to AP-XPS. The incoming X-rays are on the horizontal axis of the nozzle. B–C) Color plots of the electric potential distribution in the simulated space at the vertical axis of the nozzle (B, side view) and at the horizontal axis (C, top view).

shows the gas-phase potential between the sample and nozzle along the vertical line passing through the center of the nozzle, see Figure 6, with the data extracted from Figure 6A–D. Without an isolated patch, the gas-phase potential at the sample surface starts at 1 V and drops toward the nozzle, reaching approximately 0.4 V. The average gas-phase potential in the sampled segment in front of the sample surface is 0.96 V, that is, close to 1 V of the surface. When a small isolated patch is introduced, the gas-phase potential in close proximity to the surface is accordingly low, but due to the influence of the surrounding conducting matrix, the potential increases rapidly as a function of the distance from the sample surface. Note the broad distribution of potentials that can give rise to smeared out and broadened gas-phase peak in XPS, depending on the incident angle of the X-rays. When the patch size increases, the influence of the conducting matrix decreases. With the largest patch modeled (with a patch size larger than the aperture diameter), the gas-phase potential between the sample and nozzle never reaches 0.5 V. The average gas-phase potential for the probe volume is 0.82, 0.46, and 0.14 V, in the order of increasing patch size. Hence, with the isolated patch model we find gas-phase potential values that are larger than the surface potential.

In our last simulation (Model3), we combine the wet/dry boundary (Figure 5) with the small isolated patch (Figures 6 and 7), as shown in Figure 8. The potential distribution of the gas phase, as shown in the side view (Figure 8B), resembles that of the wet/dry boundary (Figure 5B) with the exception of the 0.5 V area (white in the color plot) starting higher as the boundary is higher and the isolated patch somewhat disturbs the potential field. The top view (Figure 8C) illustrates the latter point well but also suggests an overall more evenly distributed potential field at this horizontal cross section compared to Figure 6B without the wet/dry boundary. The average potential in the sampled segment is 0.62 V, reasonably close to the AP-XPS observation in Figure 2. The average surface potential in this case would be a convolution of the patch potential (0.02 V) and the small part of the conducting matrix, which would roughly fit the experimental observations. However, while the simulations would dictate a split of the electrolyte peak into two components, this is not observed in the experiments. Nevertheless, the model qualitatively demonstrates that the gas-phase potential can deviate from the simplified view depicted in Figure 4 in the presence of an ionically isolated surface patch (or patches) in an ionically connected matrix. Realistic conditions in a dip-and-pull experiment can vary widely in detail and complexity with a hypothetically much more inhomogeneous potential distribution over the sample surface.

Let us finish the simulation section by pointing out a few more of its limitations. In the simulations, we only introduced the gas phase between the sample and the tip of the nozzle. In reality, the gas is everywhere in the sample chamber, even inside the nozzle, with a pressure distribution which depends on the flow regime through the aperture, ranging from molecular to turbulent to viscous flow.[31,32] The binding energy shift of the gas phase at a given position is the convolution of the potential field and pressure at that position. In the simulation, we completely neglected any pressure gradient in the space between sample and spectrometer aperture. Because the pressure gradient is strong at the aperture but it is weaker in the vicinity of the sample surface (where most of the illumination by the X-rays takes place), at a typical aperture-sample distance of 1.5–2 times the aperture diameter[33] (1.67 in our simulation), the effect of neglecting the pressure gradient is then likely small.

At this point, let us turn to the samples that were used for the experiments described in Figures 2 and 3. As mentioned above, these are thin film samples and their actual thickness matters. Figure S6 provides a cross-sectional transmission electron microscopy (TEM) view of the samples and the corresponding elemental maps of Fe and Sn. The TEM investigation of sample S10 suggests a three-dimensional network of fairly round Fe_2O_3 crystallites, approximately 50–100 nm in diameter. The overall hematite film thickness was approximately 200 nm, whereas the FTO film is 500–600 nm thick and has some roughness. The surface of hematite is hydrophilic and, when immersed into the electrolyte, the small nanopores of the hematite film close to the bulk electrolyte will be filled with electrolyte. An upper part, however, may partially dry out exposing some of the hematite nanoparticles. Points on the film further from the electrolyte/meniscus might be completely dry, apart from the 2–5 ML water film by water adsorption dictated by the gas-phase water pressure. This latter water film is however not ionically well connected to the bulk electrolyte. Hence, there is a range of conditions and surface potentials expected across the sample surface. Moreover, the roughness on the nano and micrometer scale and other inhomogeneities can contribute to local differences in the wettability, with consequences for the experimental results. As shown in the lower panels of Figure S6, sample S2 has a smaller Fe_2O_3 film thickness and much reduced porosity. We

https://doi.org/10.1021/acs.jpcc.4c00113
J. Phys. Chem. C 2024, 128, 7096–7105

therefore attribute the different observations in Figures 2 and 3 to the nanomorphology of the samples and not necessarily to the electrolyte film thickness, as even with sample S10 the average electrolyte film thickness was 8 nm. We note, however, that a very thick electrolyte film that is not penetrable to photoelectrons from the sample will also provide spectral observations in line with Figures 3 and S4.

Although the O 1s spectra in combination with the COMSOL simulations convincingly show that at the measured position the potential was not as expected, and hence, changes in the spectra should not be overinterpreted, it is still worth discussing a few spectral details. With sample S10 we find a reversible change of spectral intensity at around 531.5 eV (Figure 2) when cycling between anodic and cathodic conditions. This reversible change is absent in Figure 3, when no lattice O component is visible in the dip-and-pull spectra. We know that not only the lattice O but the whole sample was absent in the XPS spectra, that is, hidden under the meniscus, because with the set shown in Figure S4 we confirmed the absence of Fe 2p. Hence, the assignment of the 531.5 eV peak to solely surface OH is wrong. Indeed, a low BE shoulder of the electrolyte peak approximately at the same position as in our work was found by Starr et al.[34] and Novotny et al.[26] Although these two studies used different electrolytes, both studies assigned the extra peak to aqueous phase ions, phosphate, and hydroxide, respectively. Novotny et al. used the same 0.1 M KOH, as we did here, and, with the assumption of homogeneous distribution of OH^- in the information depth, they calculated a 25−60 time increase of OH^- concentration in the thin electrolyte film. They concluded that this massive increase of the KOH concentration was due to a locally higher temperature (sample being in good thermal contact with the manipulator or a beam induced effect) and evaporation of water from the liquid film together with a decreased diffusion of the ions within the thin electrolyte film. This increased hydroxide concentration results in a massive shift of the pH scale in the meniscus. Because at cathodic potential the ratio of the 531.5 eV peak to lattice O is too large, see Figure 2B, both surface OH and aqueous hydroxide ions contribute to the 531.5 eV peak. Hence, the massively enhanced hydroxide concentration in the thin electrolyte film applies to our case as well. The reversible change of this peak when cycling the potential suggests a consumption of hydroxide under anodic conditions and replenishment of OH^- concentration under cathodic conditions. This makes sense, as surface OH deprotonates under anodic polarization and aqueous hydroxide reacts under the photoelectrocatalytic OER to produce O_2.[15] The slow further increase of hydroxide under repeated cathodic conditions (Figure S2E) points to a diffusion limited process with high mass transport resistance. The reason why these reversible changes of hydroxide concentration occur when the actual local potential change is likely much less than intended is currently unclear. We speculate that the process is not directly related to the potential at the measured spot; rather, while the consumption and replenishment of hydroxide at the well-connected surface parts drive these changes, it is just the diffusion across the measurement spot that we observe in the O 1s spectra of Figure 2.

An independent application of gas-phase shifts in core-level spectra are to evaluate work function changes of samples.[35] The simulations of the electric field in the gap between the sample and the aperture demonstrate that the field shows clear deviations from a simple linear dependence on the distance, even for samples with a homogeneous potential across the whole surface. The situation becomes more complicated when the potentials vary across the sample surface. For the case of a sample with homogeneous potential, meaningful information can still be obtained from gas-phase peak shifts due to, e.g., changes in the work function as a function of the experimental conditions such as due to the adsorption of molecules. The simulations presented here show that the relative position of the sample, aperture, and incident X-rays needs to be kept constant throughout the measurements to correlate gas-phase peak positions with, e.g., work function changes. This situation is different for samples with inhomogeneous potential distributions across their surface, where the interpretation of gas-phase peak shifts becomes virtually impossible without knowledge of the temporal and spatial distribution of the sample potential.

CONCLUSIONS

A hematite/FTO photoanode sample that was previously used in a mechanistic study[15] of the photoelectrochemical OER was used in a dip-and-pull AP-XPS experiment. The measurements provided an unexpected result, inasmuch as the gas-phase water O 1s core level peak shifted stronger than the electrolyte peak upon potential biasing. Moreover, a reversible consumption and replenishment of hydroxide was observed in the spectra under solar simulator irradiation upon potential cycling. To explain the unexpected core level shifts upon biasing, COMSOL simulations were performed to understand the electric potential distribution in the experiments. We show that the requirement for the unexpected larger gas-phase core level shift is the existence of ionically isolated patches in the matrix of the well-connected sample surface. The reason for the inhomogeneous sample potential can be its nanostructure. The nanopores in our 200 nm hematite film sample can form electrolyte patches that are only weakly connected to or disconnected from the bulk electrolyte. We speculate that the reversible hydroxide consumption and replenishment shown in the operando spectra are due to hydroxide diffusion across the investigated sample spot and not directly caused by the reaction at the particular measurement position and actual potential. The simulations emphasize the need for ideally nonporous and highly homogeneous samples for dip-and-pull AP-XPS experiments. This work also has implications for other types of AP-XPS experiments, especially for those that evaluate the sample work function based on gas-phase core level shifts.

ASSOCIATED CONTENT

Data Availability Statement

All data used to generate Figures 2 and 3 will be made available from the Open Research Data Repository of the Max Planck Society. Also, representative COMSOL models (Model1 and Model2) will be available.

Supporting Information

The Supporting Information is available free of charge at https://pubs.acs.org/doi/10.1021/acs.jpcc.4c00113.

Current−voltage curves of sample S10; O 1s spectra of sample S10 under various conditions; dip-and-pull O 1s spectra of sample S10; dip-and-pull O 1s and Fe 2p spectra of sample S2; line scans of the gas-phase potential as in Model2 using square type patches; TEM images and elemental mapping of sample S10 and S2; an

https://doi.org/10.1021/acs.jpcc.4c00113
J. Phys. Chem. C 2024, 128, 7096−7105

additional discussion as to how much the electrolyte peak can shift upon 1 V biasing (PDF)

AUTHOR INFORMATION

Corresponding Author

Detre Teschner − *Fritz Haber Institute of the Max-Planck-Society, Berlin 14195, Germany; Max-Planck-Institute for Chemical Energy Conversion, Mülheim an der Ruhr 45470, Germany;* orcid.org/0000-0001-5021-6748; Phone: +49 30 806214927; Email: teschner@fhi-berlin.mpg.de

Authors

Julius Plescher − *Fritz Haber Institute of the Max-Planck-Society, Berlin 14195, Germany*

Simone Piccinin − *Istituto Officina dei Materiali, Consiglio Nazionale delle Ricerche, CNR-IOM, Trieste 34136, Italy;* orcid.org/0000-0002-3601-7141

Travis E. Jones − *Theoretical Division, Los Alamos National Lab, Los Alamos, New Mexico 87545, United States*

Adnan Hammud − *Fritz Haber Institute of the Max-Planck-Society, Berlin 14195, Germany*

Franz Schmidt − *Fritz Haber Institute of the Max-Planck-Society, Berlin 14195, Germany;* orcid.org/0000-0003-0125-2704

Axel Knop-Gericke − *Fritz Haber Institute of the Max-Planck-Society, Berlin 14195, Germany; Max-Planck-Institute for Chemical Energy Conversion, Mülheim an der Ruhr 45470, Germany*

Hendrik Bluhm − *Fritz Haber Institute of the Max-Planck-Society, Berlin 14195, Germany;* orcid.org/0000-0001-9381-3155

Andrey Shavorskiy − *MAX IV Laboratory, Lund University, Lund 22484, Sweden;* orcid.org/0000-0002-7517-5089

Complete contact information is available at: https://pubs.acs.org/10.1021/acs.jpcc.4c00113

Funding

Open access funded by Max Planck Society.

Notes

The authors declare no competing financial interest.

ACKNOWLEDGMENTS

We acknowledge MAX IV Laboratory for time on the HIPPIE Beamline under proposal 20230862. Research conducted at MAX IV, a Swedish national user facility, is supported by the Swedish Research council under contract 2018-07152, the Swedish Governmental Agency for Innovation Systems under contract 2018-04969, and Formas under contract 2019-02496."

REFERENCES

(1) Echevarría, L.; Malerba, A.; Arechavala-Gomeza, V. Researcher's Perceptions on Publishing "Negative" Results and Open Access. *Nucleic Acid Ther.* **2021**, *31* (3), 185−189.

(2) Fanelli, D. Negative results are disappearing from most disciplines and countries. *Scientometrics* **2012**, *90* (3), 891−904.

(3) Song, F.; Parekh, S.; Hooper, L.; Loke, Y. K.; Ryder, J.; Sutton, A. J.; Hing, C.; Kwok, C. S.; Pang, C.; Harvey, I. Dissemination and publication of research findings: an updated review of related biases. *Health Technol. Assess.* **2010**, *14*, iii, ix−xi, 1-193.

(4) Ioannidis, J. P. Why Most Discovered True Associations Are Inflated. *Epidemiology* **2008**, *19* (5), 640−648.

(5) Song, J.; Wei, C.; Huang, Z.-F.; Liu, C.; Zeng, L.; Wang, X.; Xu, Z. J. A review on fundamentals for designing oxygen evolution electrocatalysts. *Chem. Soc. Rev.* **2020**, *49* (7), 2196−2214.

(6) Reier, T.; Nong, H. N.; Teschner, D.; Schlögl, R.; Strasser, P. Electrocatalytic Oxygen Evolution Reaction in Acidic Environments − Reaction Mechanisms and Catalysts. *Adv. Energy Mater.* **2017**, *7* (1), 1601275.

(7) Dau, H.; Limberg, C.; Reier, T.; Risch, M.; Roggan, S.; Strasser, P. The Mechanism of Water Oxidation: From Electrolysis via Homogeneous to Biological Catalysis. *ChemCatchem* **2010**, *2* (7), 724−761.

(8) Suen, N.-T.; Hung, S.-F.; Quan, Q.; Zhang, N.; Xu, Y.-J.; Chen, H. M. Electrocatalysis for the oxygen evolution reaction: Recent development and future perspectives. *Chem. Soc. Rev.* **2017**, *46* (2), 337−365.

(9) Shiva Kumar, S.; Himabindu, V. Hydrogen production by PEM water electrolysis − A review. *Mater. Sci. Energy Technol.* **2019**, *2* (3), 442−454.

(10) Jiang, C.; Moniz, S. J. A.; Wang, A.; Zhang, T.; Tang, J. Photoelectrochemical devices for solar water splitting − materials and challenges. *Chem. Soc. Rev.* **2017**, *46* (15), 4645−4660.

(11) Hunter, B. M.; Gray, H. B.; Müller, A. M. Earth-Abundant Heterogeneous Water Oxidation Catalysts. *Chem. Rev.* **2016**, *116* (22), 14120−14136.

(12) Hisatomi, T.; Kubota, J.; Domen, K. Recent advances in semiconductors for photocatalytic and photoelectrochemical water splitting. *Chem. Soc. Rev.* **2014**, *43* (22), 7520−7535.

(13) Roger, I.; Shipman, M. A.; Symes, M. D. Earth-abundant catalysts for electrochemical and photoelectrochemical water splitting. *Nat. Rev. Chem.* **2017**, *1* (1), 0003.

(14) Nong, H. N.; Falling, L. J.; Bergmann, A.; Klingenhof, M.; Tran, H. P.; Spöri, C.; Mom, R.; Timoshenko, J.; Zichittella, G.; Knop-Gericke, A.; et al. Key role of chemistry versus bias in electrocatalytic oxygen evolution. *Nature* **2020**, *587* (7834), 408−413.

(15) Righi, G.; Plescher, J.; Schmidt, F.-P.; Campen, R. K.; Fabris, S.; Knop-Gericke, A.; Schlögl, R.; Jones, T. E.; Teschner, D.; Piccinin, S. On the origin of multihole oxygen evolution in haematite photoanodes. *Nat. Catal.* **2022**, *5* (10), 888−899.

(16) Le Formal, F.; Pastor, E.; Tilley, S. D.; Mesa, C. A.; Pendlebury, S. R.; Grätzel, M.; Durrant, J. R. Rate Law Analysis of Water Oxidation on a Hematite Surface. *J. Am. Chem. Soc.* **2015**, *137* (20), 6629−6637.

(17) Mesa, C. A.; Francàs, L.; Yang, K. R.; Garrido-Barros, P.; Pastor, E.; Ma, Y.; Kafizas, A.; Rosser, T. E.; Mayer, M. T.; Reisner, E.; et al. Multihole water oxidation catalysis on haematite photoanodes revealed by operando spectroelectrochemistry and DFT. *Nat. Chem.* **2020**, *12* (1), 82−89.

(18) Zandi, O.; Hamann, T. W. Determination of photoelectrochemical water oxidation intermediates on haematite electrode surfaces using operando infrared spectroscopy. *Nat. Chem.* **2016**, *8* (8), 778−783.

(19) Braun, A.; Sivula, K.; Bora, D. K.; Zhu, J.; Zhang, L.; Grätzel, M.; Guo, J.; Constable, E. C. Direct Observation of Two Electron Holes in a Hematite Photoanode during Photoelectrochemical Water Splitting. *J. Phys. Chem. C* **2012**, *116* (32), 16870−16875.

(20) Shavorskiy, A.; Ye, X.; Karslıoğlu, O.; Poletayev, A. D.; Hartl, M.; Zegkinoglou, I.; Trotochaud, L.; Neměák, S.; Schneider, C. M.; Crumlin, E. J.; et al. Direct Mapping of Band Positions in Doped and Undoped Hematite during Photoelectrochemical Water Splitting. *J. Phys. Chem. Lett.* **2017**, *8* (22), 5579−5586.

(21) Temperton, R. H.; Kawde, A.; Eriksson, A.; Wang, W.; Kokkonen, E.; Jones, R.; Gericke, S. M.; Zhu, S.; Quevedo, W.; Seidel, R.; et al. Dip-and-pull ambient pressure photoelectron spectroscopy as a spectroelectrochemistry tool for probing molecular redox processes. *J. Chem. Phys.* **2022**, *157* (24), 244701−244701.

(22) Zhu, S.; Scardamaglia, M.; Kundsen, J.; Sankari, R.; Tarawneh, H.; Temperton, R.; Pickworth, L.; Cavalca, F.; Wang, C.; Tissot, H. I.; et al. HIPPIE: A new platform for ambient-pressure X-ray

photoelectron spectroscopy at the MAX IV Laboratory. *J. Synchrotron Radiat.* **2021**, *28* (2), 624−636.
(23) COMSOL AB COMSOL Multiphysics® V. 6.0. Www.Comsol.com; Stockholm, Sweden.
(24) Axnanda, S.; Crumlin, E. J.; Mao, B.; Rani, S.; Chang, R.; Karlsson, P. G.; Edwards, M. O. M.; Lundqvist, M.; Moberg, R.; Ross, P.; et al. Using "Tender" X-ray Ambient Pressure X-Ray Photoelectron Spectroscopy as A Direct Probe of Solid-Liquid Interface. *Sci. Rep.* **2015**, *5* (1), 9788.
(25) Crumlin, E. J.; Liu, Z.; Bluhm, H.; Yang, W.; Guo, J.; Hussain, Z. X-ray spectroscopy of energy materials under in situ/operando conditions. *J. Electron Spectrosc. Relat. Phenom.* **2015**, *200*, 264−273.
(26) Novotny, Z.; Aegerter, D.; Comini, N.; Tobler, B.; Artiglia, L.; Maier, U.; Moehl, T.; Fabbri, E.; Huthwelker, T.; Schmidt, T. J.; et al. Probing the solid-liquid interface with tender x rays: A new ambient-pressure x-ray photoelectron spectroscopy endstation at the Swiss Light Source. *Rev. Sci. Instrum.* **2020**, *91* (2), 023103.
(27) Favaro, M.; Clark, P. C. J.; Sear, M. J.; Johansson, M.; Maehl, S.; van de Krol, R.; Starr, D. E. Spectroscopic analysis with tender X-rays: SpAnTeX, a new AP-HAXPES end-station at BESSY II. *Surf. Sci.* **2021**, *713*, 121903−121903.
(28) Nikjoo, H.; Uehara, S.; Emfietzoglou, D.; Brahme, A. Heavy charged particles in radiation biology and biophysics. *New J. Phys.* **2008**, *10* (7), 075006.
(29) Emfietzoglou, D.; Nikjoo, H. Accurate Electron Inelastic Cross Sections and Stopping Powers for Liquid Water over the 0.1-10 keV Range Based on an Improved Dielectric Description of the Bethe Surface. *Radiat. Res.* **2007**, *167* (1), 110−120.
(30) Favaro, M.; Yang, J.; Nappini, S.; Magnano, E.; Toma, F. M.; Crumlin, E. J.; Yano, J.; Sharp, I. D. Understanding the Oxygen Evolution Reaction Mechanism on CoOx using Operando Ambient-Pressure X-ray Photoelectron Spectroscopy. *J. Am. Chem. Soc.* **2017**, *139* (26), 8960−8970.
(31) Kahk, J. M.; Villar-Garcia, I. J.; Grechy, L.; Bruce, P. J. K.; Vincent, P. E.; Eriksson, S. K.; Rensmo, H.; Hahlin, M.; Åhlund, J.; Edwards, M. O. M.; et al. A study of the pressure profiles near the first pumping aperture in a high pressure photoelectron spectrometer. *J. Electron Spectrosc. Relat. Phenom.* **2015**, *205*, 57−65.
(32) Ogletree, D. F.; Bluhm, H.; Lebedev, G.; Fadley, C. S.; Hussain, Z.; Salmeron, M. A differentially pumped electrostatic lens system for photoemission studies in the millibar range. *Rev. Sci. Instrum.* **2002**, *73* (11), 3872−3877.
(33) Bluhm, H. Photoelectron spectroscopy of surfaces under humid conditions. *J. Electron Spectrosc. Relat. Phenom.* **2010**, *177* (2), 71−84.
(34) Starr, D. E.; Favaro, M.; Abdi, F. F.; Bluhm, H.; Crumlin, E. J.; van de Krol, R. Combined soft and hard X-ray ambient pressure photoelectron spectroscopy studies of semiconductor/electrolyte interfaces. *J. Electron Spectrosc. Relat. Phenom.* **2017**, *221*, 106−115.
(35) Axnanda, S.; Scheele, M.; Crumlin, E.; Mao, B.; Chang, R.; Rani, S.; Faiz, M.; Wang, S.; Alivisatos, A. P.; Liu, Z. Direct Work Function Measurement by Gas Phase Photoelectron Spectroscopy and Its Application on PbS Nanoparticles. *Nano Lett.* **2013**, *13* (12), 6176−6182.

https://doi.org/10.1021/acs.jpcc.4c00113
J. Phys. Chem. C 2024, 128, 7096−7105